Spatial and temporal variability of meteorological variables at Haut Glacier d'Arolla (Switzerland) during the ablation season 2001: Measurements and simulations

Ulrich Strasser
Department of Earth and Environmental Sciences, Section Geography, University of Munich, Germany

Javier Corripio, Francesca Pellicciotti, and Paolo Burlando
Institute of Hydromechanics and Water Resources Management, Section Hydrology and Water Resources Management, ETH Zurich, Switzerland

Ben Brock
Department of Geography, University of Dundee, Scotland

Martin Funk
Laboratory of Hydraulics, Hydrology and Glaciology, Section Glaciology, ETH Zurich, Switzerland

Received 14 July 2003; revised 24 November 2003; accepted 26 November 2003; published 5 February 2004.

[1] During the ablation period 2001 a glaciometeorological experiment was carried out on Haut Glacier d'Arolla, Switzerland. Five meteorological stations were installed on the glacier, and one permanent automatic weather station in the glacier foreland. The altitudes of the stations ranged between 2500 and 3000 m a.s.l., and they were in operation from end of May to beginning of September 2001. The spatial arrangement of the stations and temporal duration of the measurements generated a unique data set enabling the analysis of the spatial and temporal variability of the meteorological variables across an alpine glacier. All measurements were taken at a nominal height of 2 m, and hourly averages were derived for the analysis. The wind regime was dominated by the glacier wind (mean value 2.8 m s^{-1}) but due to erosion by the synoptic gradient wind, occasionally the wind would blow up the valley. A slight decrease in mean 2 m air temperatures with altitude was found, however the 2 m air temperature gradient varied greatly and frequently changed its sign. Mean relative humidity was 71% and exhibited limited spatial variation. Mean incoming shortwave radiation and albedo both generally increased with elevation. The different components of shortwave radiation are quantified with a parameterization scheme. Resulting spatial variations are mainly due to horizon obstruction and reflections from surrounding slopes, i.e., topography. The effect of clouds accounts for a loss of 30% of the extraterrestrial flux. Albedos derived from a Landsat TM image of 30 July show remarkably constant values, in the range 0.49 to 0.50, across snow covered parts of the glacier, while albedo is highly spatially variable below the zone of continuous snow cover. These results are verified with ground measurements and compared with parameterized albedo. Mean longwave radiative fluxes decreased with elevation due to lower air temperatures and the effect of upper hemisphere slopes. It is shown through parameterization that this effect would even be more pronounced without the effect of clouds. Results are discussed with respect to a similar study which has been carried out on Pasterze Glacier (Austria). The presented algorithms for interpolating, parameterizing and simulating variables and parameters in alpine regions are integrated in the software package AMUNDSEN which is freely available to be adapted and further developed by the community. *INDEX TERMS:* 1827 Hydrology: Glaciology (1863); 1833 Hydrology: Hydroclimatology; 1863 Hydrology: Snow and ice (1827); *KEYWORDS:* Spatial and temporal variability, glacier climate, radiation modeling, albedo parameterization, Landsat TM, AMUNDSEN

Citation: Strasser, U., J. Corripio, F. Pellicciotti, P. Burlando, B. Brock, and M. Funk (2004), Spatial and temporal variability of meteorological variables at Haut Glacier d'Arolla (Switzerland) during the ablation season 2001: Measurements and simulations, *J. Geophys. Res.*, *109*, D03103, doi:10.1029/2003JD003973.

Copyright 2004 by the American Geophysical Union.
0148-0227/04/2003JD003973$09.00

1. Introduction

[2] Between May and September of 2001 a glaciometeorological experiment was carried out at Haut Glacier d'Arolla, an alpine valley glacier in the Val d'Hérens (Switzerland). To study the spatial and temporal variability of the processes which govern the melt of snow and ice, five automatic weather stations (AWSs) were established along two intersecting transects in the central area of the glacier, distributed over elevations ranging from 2813 to 3005 m a.s.l. In addition, measurements were recorded with a permanent AWS situated in the proglacial area in 1 km distance from the glacier snout, at 2504 m a.s.l.

[3] This paper deals with the spatial and temporal patterns of the measured 2 m wind speed and direction, temperature, humidity, surface fluxes of incoming short- and longwave radiation, and surface albedo, the latter being measured directly, derived from Landsat TM satellite data and parameterized. These variables have often been measured on glaciers, but rarely have they been simultaneously recorded at more than two locations on an alpine glacier, the study by *Greuell et al.* [1997] for the Pasterze, Austria's largest glacier, being a noteable exception. For comparison, we adopt the principles of their analysis for our study and discuss the differences between the findings for the Pasterze and Haut Glacier d'Arolla.

[4] First, the average values of variables are analyzed to determine their dependence on elevation and location. Then an attempt is made to explain the observed spatial and temporal patterns of variation. For the incoming short- and longwave radiation we apply a parameterization scheme to separate relevant processes from each other.

[5] The understanding of the temporal and spatial variations of meteorological variables is a prerequisite for the description of the relation between climate and the mass balance of glaciers. The amount of surface melting is usually calculated by means of energy balance models or temperature index models. Deterministic models, the parameters of which can be estimated from available real world characteristics, have the advantage that they can be applied for the prediction of glacier evolution under future climate scenarios, since no calibration of parameters with measured data is required [*Klemes*, 1985]. Furthermore, they are applicable independently from the location. Nowadays, a broad variety of such sophisticated models is available to simulate glacier melt [*Arnold et al.*, 1996; *Brock et al.*, 2000a; *Greuell and Smeets*, 2001; *Klok and Oerlemans*, 2002], and increasing efforts are invested into the tasks of regionalization and exploiting the existing data sources for distributed model applications [*Greuell and Böhm*, 1998; *Blöschl*, 1999]. The spatial and temporal variability of meteorological variables relevant for the accumulation and ablation processes of a glacier are usually extrapolated from measurements available at a single station in the glacier area or from observations available at stations in the surrounding areas. For the distribution of these variables from a local measurement to the area of the glacier many methods of varying sophistication are generally applied:

[6] *Temperature* is often indicated as the most important variable for the determination of snow- and ice melt [see, e.g., *Ohmura*, 2001], and probably the most readily available from operational observation networks [*Hock*, 1998]. Its relative homogeneity allows for quite reliable interpolation if a representative number of stations is available. Many model applications assume a constant vertical temperature lapse rate for all conditions, ranging from -0.0055 to $-0.0065°C\ m^{-1}$ [e.g., *Hock*, 1998; *Brock et al.*, 2000a]. On the other hand, measurements show that the temperature lapse rate can vary considerably depending on the meteorological conditions (mainly cloudiness) and on effects due to topography. Taking this into account, *Escher-Vetter* [2000] uses diurnally variable lapse rates for three ranges of cloudiness and $-0.006°C\ m^{-1}$ for rainy days. *Greuell et al.* [1997] showed for Pasterze Glacier in Austria that a linear function of potential temperature against distance along the glacier gives a much better description of 2 m temperature observations than the usually assumed constant decrease of the temperature with elevation.

[7] The *phase of the precipitation* also plays an important role for the energy balance of the glacier surface, essentially during the melting season, both in terms of increasing albedo due to snowfalls (and thus reducing the net shortwave radiation flux) and the input of sensible heat energy by rain. Usually, solid/liquid precipitation transition is a fixed threshold temperature ranging between +1 and +2°C [*Hock*, 1998; *Brock et al.*, 2000a; *Escher-Vetter*, 2000; *Klok and Oerlemans*, 2002].

[8] Global radiation, i.e., the sum of direct and diffuse radiative fluxes on a horizontal surface, is the most important energy source for snow- and ice melt for alpine conditions [*Hock*, 1998]. Today, digital elevation models and sophisticated algorithms are used in distributed energy balance glacier melt models to simulate its temporal and spatial variability by incorporating the interaction with the local terrain [e.g., *Arnold et al.*, 1996, *Brock et al.*, 2000a, *Klok and Oerlemans*, 2002]. Under cloudless conditions, shortwave radiation can be reliably simulated using a high resolution digital terrain model and considering the exact position of the sun as well as the attenuation of the radiation by the atmosphere [*Garnier and Ohmura*, 1968; *Kondratyev*, 1969; *Iqbal*, 1983; *Corripio*, 2003].

[9] Incoming longwave radiation from the atmosphere is usually estimated with empirical relations based on standard meteorological measurements and using the correlation of the air temperature with vapour pressure at screen level [*Kondratyev*, 1969; *Ohmura*, 2001]. *Longwave emission* is generally calculated applying the Stefan Boltzmann law, assuming that the radiative characteristics of snow and ice are similar to those of a black body.

[10] Both temperature lapse rate and the longwave radiation are affected by *cloudiness*. Measurements from a local station are generally necessary, as the cloud cover is spatially highly variable and cannot easily be interpolated, especially in mountainous regions. The influence of cloudiness on the increase of longwave radiation is therefore generally simulated by means of empirical formulas [*Ångström*, 1916; *Brunt*, 1932; *Brutsaert*, 1975] and applying correction coefficients to account for the type of cloud cover, e.g. following the classification by *Bolz* [1999].

[11] *Wind* speed and direction also play an important role with respect to both the redistribution of precipitation and interchange of momentum and heat with the surface. However, the synoptic wind field differs from the local conditions

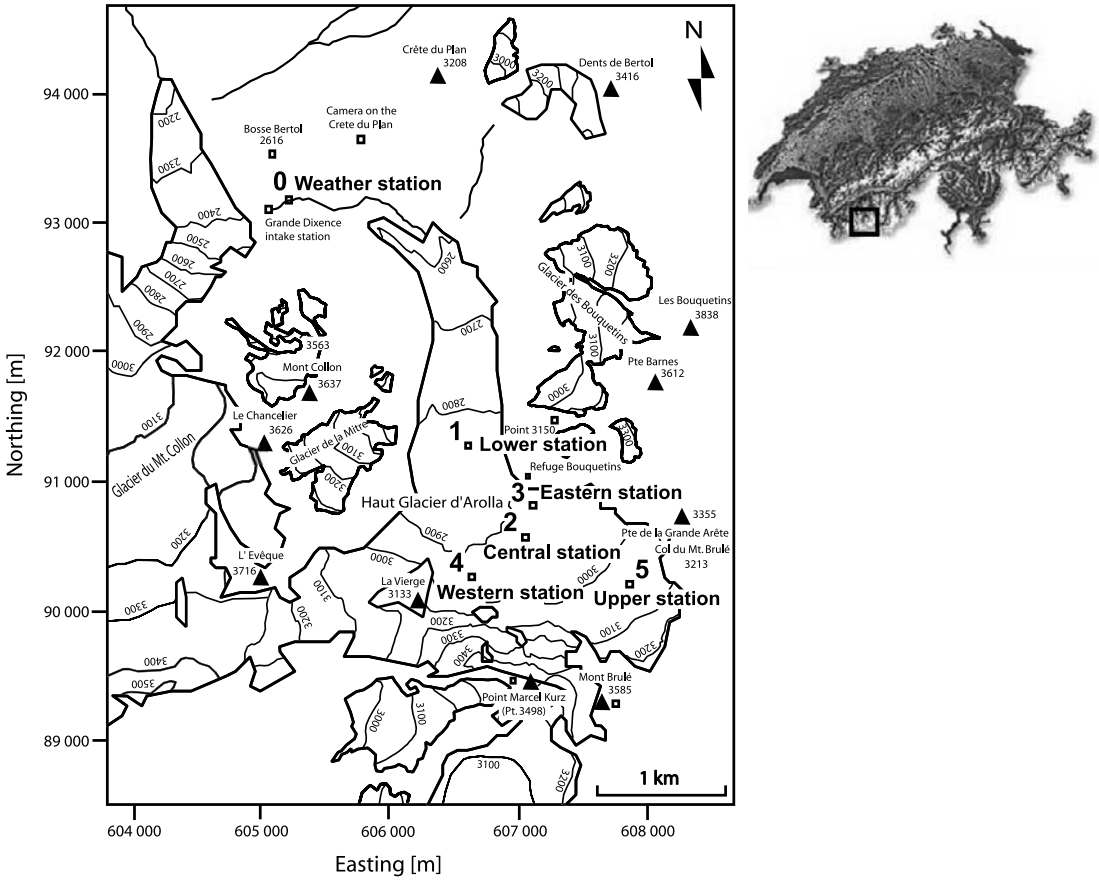

Figure 1. The catchment of the Haut Glacier d'Arolla in southern Valais (Switzerland). The meteorological stations located on the glacier were operating from end of May to beginning of September 2001. The stations are: in the glacier foreland the permanent weather station (0), and on the glacier the lower station (1), central station (2), eastern station (3), western station (4) and upper station (5). Easting and northing according to the Swiss national coordinate system.

on the glacier: the influence of the cold snow or ice surface, boundary layer effects and topographic disturbances produce a local wind field. Methods to determine the turbulent fluxes should therefore relate the conditions of the free atmosphere to the glacier wind [*Greuell and Böhm*, 1998; *Oerlemans and Grisogono*, 2000].

[12] Finally, *humidity* influences the emittance of longwave radiation from the atmosphere and controls the latent heat flux. As for the wind, humidity at the local scale differs from the synoptic field due to topography and the effect of the glacier wind, especially under melting conditions.

[13] In the following sections, the distributions of the meteorological measurements are discussed, a parameterization for the fluxes of the incoming short- and longwave radiation is developed and methods for describing the temporal and spatial variation of the surface albedo are discussed. The data analyses and parameterization schemes which are described may contribute to the further development of the existing glacier modeling approaches.

2. Experimental Setup

[14] The study site is the Haut Glacier d'Arolla, situated at the head of the Val d'Hérens, a tributary of the Rhône valley, in southern Valais (Switzerland). The glacier has an area of 4.5 km^2, is about 4 km long and comprises two upper basins lying at about 3000 m a.s.l. which combine to feed a glacier tongue extending down to about 2560 m a.s.l. (Figure 1). Slopes are generally gentle, except in the upper southeast basin where the glacier is fed by a series of steep icefalls rising up to 3500 m a.s.l. on the north face of Mont Brulé (3585 m a.s.l.). The glacier is surrounded by the Bouquetins ridge (3838 m a.s.l.) to the east and the mountains of L'Évêque (3716 m a.s.l.) and Mont Collon (3637 m a.s.l.) to the west, which are important to the glacier's radiation budget. Over the last decade the altitude of the equilibrium line has been well above 2800 m a.s.l. [*Oerlemans et al.*, 1998], leading to a strong negative mass balance with about 2.5 to 3 m a^{-1} water equivalent (w.e.) of surface ablation across the lower tongue and more than 100 m of retreat since 1989 [*Hubbard et al.*, 1998].

[15] Five meteorological stations were established along two intersecting transects in the central area of the glacier, distributed over elevations ranging from 2813 m a.s.l. to 3005 m a.s.l. (Figure 1). In addition, a permanent AWS (Station 0) has been operating since November 2000 in the proglacial area at 2504 m a.s.l., at approximately 1 km distance from the glacier snout. The lower (1), central (2) and upper (5) stations were placed on the central flow line of the glacier, whereas the eastern (3) and western (4)

Table 1. Characteristics of the Permanent Automatic Weather Station in the Proglacial Area and the Five Meteorological Stations on the Glacier

Station	Elevation, m a.s.l.	Variables Measured	Period
0 (Proglacial)	2504	Q, G, R, T, u, d, U, p	Since 28 Nov. 2000
1 (Lower)	2813	G, R, T, u, d, U	16 May to 21 June, 18 July to 12 Sep. 2001
2 (Central)	2912	Q, G, R, T, u, d, U	29 May to 6 July, 17 July to 12 Sep. 2001
3 (Eastern)	2911	G, R, T, u, d, U	16 May to 6 July, 17 July to 12 Sep. 2001
4 (Western)	2909	G, R, T, u, d, U	29 May to 12 Sep. 2001
5 (Upper)	3005	G, R, T, u, d, U	16 May to 12 Sep. 2001

Q, net total radiative flux; G, incoming shortwave radiation flux; R, outgoing shortwave radiation flux; T, air temperature; u, wind speed; d, wind direction; U, relative humidity; p, precipitation. The nominal height of the sensors is 2 m. Symbology is consistent with *Greuell et al.* [1997].

stations were set up along a horizontal line with the central station, in an altitude of about 2910 m a.s.l., to observe cross-glacier changes in the meteorological variables independent from elevation. This arrangement of the stations provides a picture of the along-glacier and traversal changes in the meteorological conditions associated with topography and surface conditions. During the late ablation period, the mean transient snow line retreated upglacier beyond Stations 1, 2 and 3, while Stations 4 and 5 remained on snow throughout the measurement period.

[16] At all locations, temperature and humidity (shielded and ventilated), wind speed and direction as well as the shortwave radiation fluxes were measured. At the central site, net radiation fluxes were measured using a net radiometer, and the lowering of the glacier surface was continuously monitored using an ultrasonic distance sensor. All measurements were taken every five seconds and five minute averages were stored on programmable dataloggers. From these, hourly means were derived for the analysis. In addition, snow surface lowering at ablation stakes and density measurements (to determine the snow w.e.) as well as albedo, temperature and humidity readings were taken periodically by hand at 28 locations on the glacier. Table 1 gives the elevations and the variables that were measured at the different station locations. The elevations of the stations are taken from the corresponding pixel of the DEM (10 m resolution) which was photogrammetrically derived from a series of aerial photographs, representing the elevation of the glacier surface in 1999 (Figure 2).

[17] The meteorological sensors were mounted on arms attached to a tripod apparatus which stood freely on the glacier surface, ensuring that the surface fluxes are measured in a surface parallel plane. Instruments were positioned at a nominal height of 2 m, however, the stations sunk in the snow approximately 0.2 m until they reached an equilibrium state; after which they continued to move downward at the same rate as the lowering of the surface due to melting, thus maintaining the distance between the instruments and the surface. In the later ablation period the Stations 1, 2 and 3 touched down on the ice, but remained stable.

[18] Before the experiments, all sensors were calibrated by the manufacturers. Technical details of the sensors are given in Table 2.

[19] For the following analyses, we use the hourly aggregated measurements which were recorded by all stations between 1 June and 31 August. On 7 July in the early morning hours a severe storm blew over Stations 2 and 3. They were repaired on 17 July. Station 1 failed beween 21 June and 18 July. These periods of missing data are not used for any analysis. Thus the number of hourly records which represent the common data base for the analysis is 1562 (unless stated otherwise - see Table 3).

[20] For the interpretation of the results, data from the meteorological stations Les Attelas (2733 m a.s.l.) and Gornergrat (3120 m a.s.l.) of MeteoSwiss will also be used, located 35 km northwest and 20 km east of Haut Glacier d'Arolla, respectively.

3. Results and Discussion

[21] The following results are all based on hourly means which are derived by aggregating the five minute averages as stored in the dataloggers. All data were checked and corrected for physical plausibility (e.g., by setting an observed relative humidity of 100.1% to 100.0%). Only variables recorded simultaneously at all stations are analysed, except longwave radiative fluxes, which were measured only at Stations 0 and 2.

3.1. Wind Field

[22] The glacier wind develops over slopes of melting snow or ice if the temperature of the adjacent air is above 0°C. Then, due to the exchange of sensible heat with the surface, the lowest wind layer cools, becomes denser and flows down the glacier due to gravity. This glacier wind determines the local wind field near the surface together with the geostrophic and valley winds which are due to radiative heating or cooling of slopes and the effect of local topography [*Greuell et al.*, 1997].

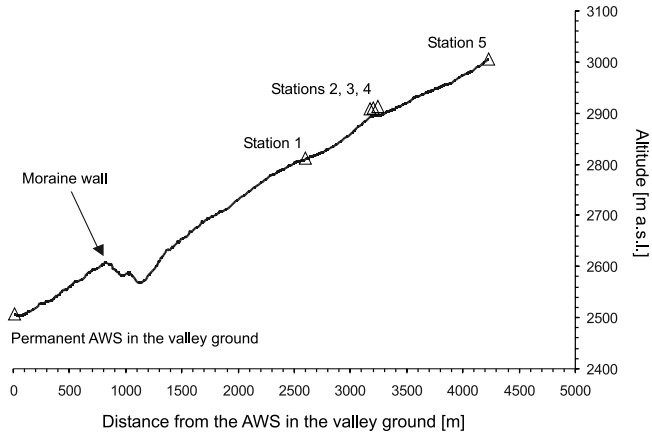

Figure 2. Profile of Haut Glacier d'Arolla along the center flow line with the locations of the meteorological stations. Stations 3 and 4 are situated some 100 m north and west of the central station (2).

Table 2. Meteorological Sensors Used for the Glaciometeorological Experiment on Haut Glacier d'Arolla 2001 and Some of Their Technical Details

Variable Measured	Manufacturer	Type	Accuracy	Range
Q	Kipp and Zonen	NR Lite	±15%	0.2 to 100 μm
G, R	Kipp and Zonen	CM 7B	±5%	305 to 2800 nm
T, U	Rotronic	MP103A	±1%, ±0.3°C	0 to 100%, −40 to +60°C
u, d	Young	S-WMON	±0.3 m s^{-1}, ±3°	1 to 60 m s^{-1}
p	Ott	Pluvio 1000	<0.4%	0 to 50 mm min^{-1}

[23] During the period of our observations, the wind regime was characterized by the glacier wind at all stations. As an example, at Station 3 the predominant wind direction is E or SE for approximately 60% of the recordings (Figure 3, left). Even at Station 0 in the glacier foreland, about one kilometer away from the glacier snout, easterly wind directions were observed in approximately 50% of the recordings. Owing to the vicinity of a hill (Bosse Bertol, 2616 m a.s.l.) the proglacial area is protected against the synoptic gradient field. There (at Station 0), SW slope winds from the north face of Mont Collon (3637 m a.s.l.) are frequently recorded (40%).

[24] Mean wind speed for all stations was around 2.8 m s^{-1} and decreased with elevation from 3.5 (Station 1) to 2.5 (Station 5) m s^{-1}. *Greuell et al.* [1997] found a smaller variation at the Pasterze Glacier, but there the mean wind speed was around 4 m s^{-1}. In our data, the increase in wind speed in moving down-glacier is not strengthened when only katabatic flows are considered, i.e., wind directions with an easterly or southerly component (katabatic flow conditions were selected by limiting the range of wind directions to angles from 45° to 225°): then, mean wind speed is 3.1 (Station 1) and 2.1 (Station 5) m s^{-1}, respectively. The spatial variation in wind speed, related to the meteorological conditions during the experiment or the topography of the glacier and its surrounding, may be a combination of the following effects: (1) the smaller fetch of the glacier wind in the upper areas; (2) the smaller temperature contrast between the glacier surface and the ambient atmosphere at higher elevations, i.e., smaller katabatic forces; and (3) the fact that because of the relatively open landscape in the upper areas, the synoptic wind can more easily erode the glacier wind, whereas the lower valley is comparably narrow, leading to convergence acceleration of the wind flow. An attempt to relate the 2 m wind speed to 2 m temperature to test whether the speed of the glacier wind increases with air temperature did not lead to any conclusive results, as for Pasterze Glacier [*Greuell et al.*, 1997].

[25] Highest wind speeds over 10 m s^{-1} (hourly mean) occurred under synoptic-scale forcing and had a north-westerly component, whereas the local glacier wind with a south-easterly component only reached speeds up to 7 m s^{-1} (Figure 3, right). Similar results were obtained for all stations on the glacier, except Station 4 where southerly wind directions were predominant in approximately 85% of the recordings. This was probably due to its specific location, distant from the glacier center flow line, at the foot of a steep north facing slope (Figure 1). At Station 4 mean wind speed was lowest (Table 3). The maximum hourly mean wind speed of 12 m s^{-1} was observed at Station 1 on the glacier tongue on 3 June.

[26] Directional constancy (see Table 3), defined as the ratio of the time averaged wind vector to the time averaged wind speed, is highest at Station 4 (0.49), where topography most strongly controls the local wind regime, and lowest at Station 5 (0.15). This can be explained by the fact that, at Station 5, the fetch is roughly equal for gravity driven flows from northerly, southerly and easterly directions (Figure 1), leading to fairly weak katabatic winds of variable orientation.

[27] In general, the values of the directional constancies are much lower than the ones observed by *Greuell et al.* [1997] for the Pasterze Glacier. There, the orientation of the glacier long axis is the same as the direction of the prevailing synoptic wind flow (NW to SE), whereas at Haut Glacier d'Arolla, the glacier long axis is directly opposed to the prevailing synoptic winds, leading to frequent changes of the observed wind direction. Furthermore, at the tongue of Pasterze Glacier the downvalley directivity, defined as the ratio of the mean downvalley component of the wind to the mean wind speed, never became negative which means that the resulting daily wind vector always had a downvalley component [*Greuell et al.*, 1997]. In contrast, at Haut Glacier d'Arolla frequent negative downvalley directivities were observed (Figure 4), indicating that up-glacier winds dominated on particular days. This situation complicates the distinction between the synoptic and the valley wind, in particular for situations with frequent wind direction changes at low wind speeds.

[28] Wind speed frequency distributions were found to be all positively skewed at the different stations, whereas

Table 3. Averages of the Meteorological Variables Measured at Haut Glacier d'Arolla During the Period 1 June to 31 August 2001

Meteorological Variable	Nr. of Hourly Means	Station					
		Proglacial (0)	Lower (1)	Central (2)	Eastern (3)	Western (4)	Upper (5)
Directional constancy	1562	0.30	0.37	0.41	0.23	0.49	0.15
2 m wind speed, m s^{-1}	1562	2.8	3.5	2.6	3.0	2.3	2.5
2 m temperature, °C	1562	5.8	2.8	2.6	2.8	3.0	2.4
2 m relative humidity, %	1562	72	73	72	74	64	71
Incoming shortwave radiation, W m^{-2}	1562	247	250	263	270	245	272
Incoming longwave radiation, W m^{-2}	1951	294	-	279	-	-	-

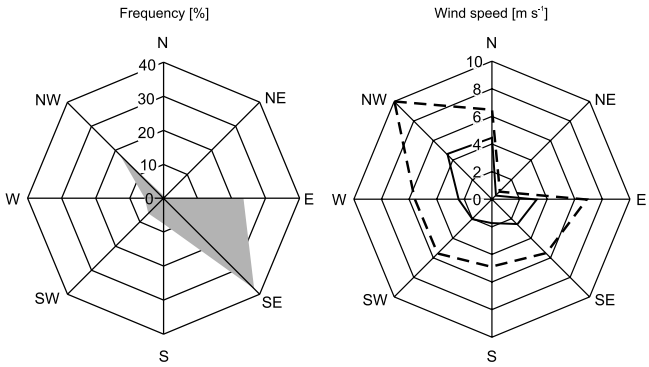

Figure 3. Hourly measured 2 m wind direction frequency (left) and wind speed-direction distribution (right) at station 3. The solid line denotes mean wind speed, and the dashed line denotes maximum wind speed.

Greuell et al. [1997] found greater variability at Pasterze Glacier with a very skewed distribution near the crest, and a normal distribution, i.e., almost continuous katabatic forcing, on the glacier tongue. There, the lower stations are much better protected against storm events with synoptic wind directions than at Haut Glacier d'Arolla. For quantitative comparison with the results for the Pasterze Glacier, we fitted the same two parameter Weibull distribution function [*Justus et al.*, 1978] to our data:

$$F(U) = 1 - e^{\left[-\left(\frac{U}{a}\right)^{k_w}\right]} \quad (1)$$

where F(U) is the probability that the wind speed is less than U, and a and k_w are free parameters. Figure 5 shows the best fit to the data at Station 3. For the other stations, the distributions look quite similar.

3.2. Temperature

[29] Figure 6 shows the comparatively much lower mean 2 m temperatures over snow and ice (Stations 1 to 5) than at Station 0 and the two meteorological stations Les Attelas and Gornergrat of MeteoSwiss (which record the "free atmosphere temperature"), due to the cooling effect of the melting glacier surface. However, Station 0 is situated in the center of the valley beneath the glacier and thus in the sphere of influence of the katabatic flow from the glacier: even though the station is situated more than 200 m lower, the mean temperature was only slightly higher than at Les Attelas (0.1°C).

[30] On the glacier the mean temperature decreased, as generally expected, more or less linearly with elevation from Station 1 to 2 to 5. At Stations 3 and 4, outside the main flow of the katabatic glacier wind, somewhat higher temperatures than at Station 2 were recorded (the elevation difference between Stations 2, 3 and 4 is negligible). The observed temperature distribution can be explained following *Greuell et al.* [1997]. The main relevant processes for the temperature in the glacier wind layer are adiabatic heating of descending air and exchange of sensible heat with the underlying surface; differences in the observed temperature patterns due to entrainment, phase changes and radiation divergence can be neglected. On gentle slopes, as at Haut Glacier d'Arolla, the exchange of sensible heat dominates the adiabatic heating, leading to the mean measured decrease of temperature with elevation of $-0.002°C\ m^{-1}$. On steep slopes, however, adiabatic heating dominates and the lapse rate may approach the atmospheric dry adiabatic lapse rate. The relatively high mean temperature at Station 4 can therefore be explained by its position at the bottom of a steep slope (Figure 1) and the pronounced heating of the downflowing winds. Whereas, Station 3 is close to a south facing moraine slope which becomes snowfree much earlier than the glacier itself at that altitude, and therefore the air is warmed by turbulent transfer of sensible heat and longwave radiation.

[31] In the extrapolation of 2 m temperature across glaciers, other effects should be considered as well, e.g., both convergence and divergence of the flow and non-glacier winds have their influence on the spatial temperature distribution. To some extent these processes might compensate for each other. The consequences of such effects is beyond the scope of this paper, but treated in detail by *Greuell and Böhm* [1998]. At Haut Glacier d'Arolla, the temperature gradient between Stations 1 and 5 frequently changed its sign and varied between $-0.0126°C\ m^{-1}$ and $+0.0231°C\ m^{-1}$ (Figure 7). Temperature inversions (i.e., an increase with increasing elevation) can be observed when the glacier surface atmospheric layer is poorly developed and shallower than 2 m. This is more likely to occur at Station 5 where the fetch is very short. Under such conditions, Station 5 will effectively record the 'free atmosphere' temperature which is higher than the glacier surface layer temperature at Stations 2 and 1. Although these two stations are at lower elevations, they have a larger fetch for katabatic flows and therefore a deeper surface atmospheric layer. In the later melting season (July/August), such occurences are more pronounced than in the beginning (June) due to the generally higher air temperatures. Still, in 72% of the recordings the gradient is negative (lower temperature at higher elevation), in 28% it is positive (higher temperature in higher elevation - Figure 8).

[32] The variations of the temperature gradient can be considered for glacier melt modeling when at least two stations at different altitude on the glacier are available.

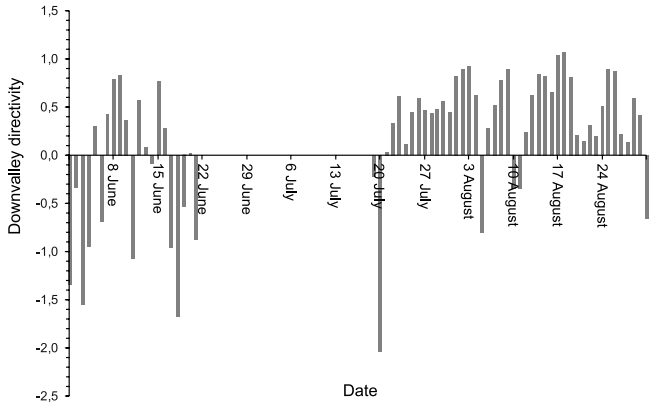

Figure 4. Downvalley directivities at station 3 for summer 2001. The lowest alues are due to strong northerly air streams which erode the glacier wind. One of these events destroyed the station on 21 June. It was then out of order until 17 July.

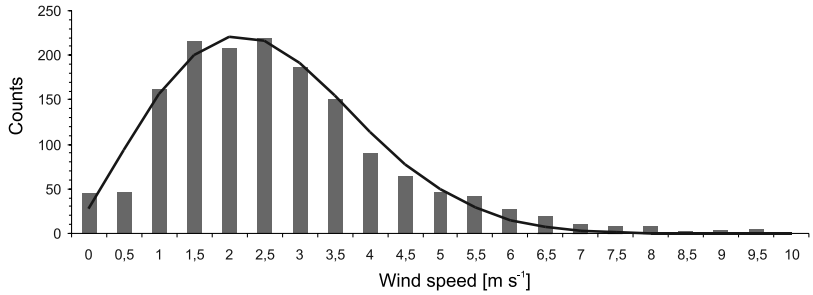

Figure 5. Hourly mean 2 m wind speed distribution at station 3 and two parameter Weibull distribution function, being a = 3.18 and k_w = 2.18.

Fields of temperature or any other meteorological variable can then be applicatively provided with high temporal resolution applying the following procedure [*Strasser and Mauser*, 2001]: first, a so-called *gradient field* is derived by linear regression of the meteorological observations with altitude; this regression is then applied for the entire area represented by the DEM. Then, the residuals (i.e., the deviations of the measurements from the gradient field) are spatially interpolated applying an inverse distance weighting (IDW) approach, resulting in the so-called *residual field* representing the local deviations from the gradient field. The weights are the distances between a location represented by a DEM pixel and the stations. In a last step, gradient and residual field are added up. This algorithm, applied for each time step, ensures that the station observations are reproduced, and it can be applied irrespective of whether a relation of the meteorological variable with altitude or local deviations exist (then, a field of zeros is added without consequence). Only extrapolations beyond the network of stations or out their range of altitudes should be interpreted with caution. An example for an interpolated field with both variances, in elevation and locally, is shown in Figure 9. One can see that the temperature pattern reproduces the expected distribution with lower temperatures in higher elevations, according to the DEM, but there are also deviations of the measurements from the gradient field, recognizable as a dark area around Station 1 and a bright area around Station 4: at Station 1 the recorded temperature is lower than the computed gradient field, whereas at Station 4 it is higher. With the variable gradient all kinds of meteorological conditions can be appropriately modelled, being synoptic or local effects.

[33] To test the interpolation scheme, the procedure has been applied to our data set without the measurements at the central station, allowing for their comparison with the interpolated variables for this site. The comparison shows good agreement, resulting in efficiencies of R^2 = 0.98 (temperature and shortwave radiation), R^2 = 0.97 (relative humidity) and R^2 = 0.78 (wind speed). Efficiency was thereby calculated after *Nash and Sutcliffe* [1970]:

$$R^2 = 1 - \frac{\sum(v_{obs} - v_{sim})^2}{\sum(v_{obs} - \bar{v}_{obs})^2} \tag{2}$$

where v_{obs} are the observed (being $\bar{v}_{obs}$ their mean) and v_{sim} the estimated values.

3.3. Humidity

[34] As can be seen in Table 3, the relative humidity did not significantly change with elevation. At Station 4 it was considerably lower, however. There, southerly directions with adiabatic heating of descending air dominated the local wind in more than 80% of the recordings, and advected dry air from icefree ground. Temporal variations of humidity were of much greater significance than the local ones, ranging from 9% (5 June at Station 4) to 100% (31 August at Station 0).

3.4. Shortwave Radiation

[35] The global radiation (G) varied considerably from site to site (see Table 3). In general, G increased with

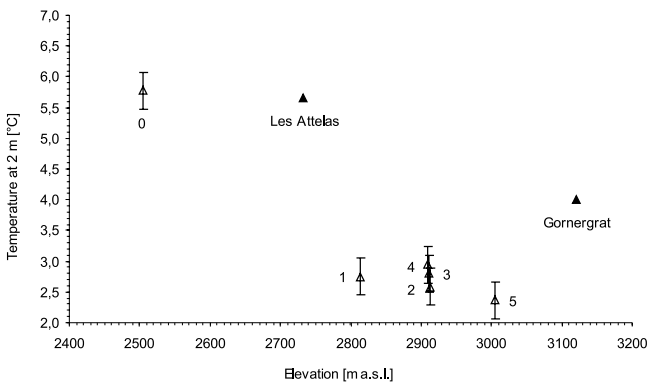

Figure 6. Mean 2 m temperature against elevation for Station 1 to 5 on the glacier, for Station 0 in the proglacial area and for Les Attelas (2733 m a.s.l.) as well as Gornergrat (3120 m a.s.l.) of MeteoSwiss. An accuracy of ±0.3°C is given by the error bars (see Table 2).

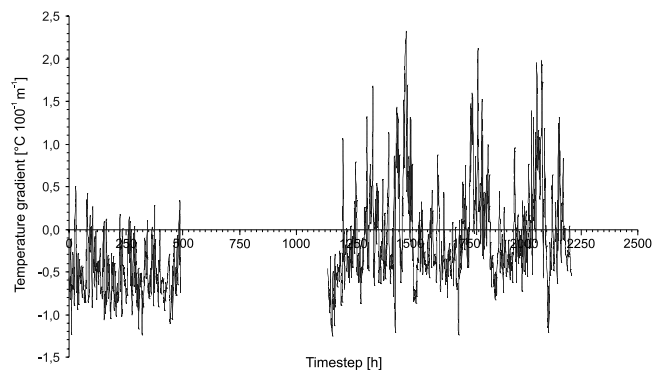

Figure 7. Temperature gradient for hourly measurements between stations 1 and 5 on Haut Glacier d'Arolla.

elevation, with a maximum at the highest Station (5). At Station 4, the lowest value of G is due to the shading effect of the nearby peak of La Vierge (Figure 1).

[36] At the top of the atmosphere, the shortwave radiative fluxes would be the same for all stations, since the latitudinal differences between them are negligible. On the ground, the differences are caused by several elevation dependent atmospheric processes and the effect of topography: (1) loss due to Rayleigh and aerosol scattering and absorption by water vapour, ozone and other trace gases, and (2) gain due to multiple reflections between the atmosphere and the ground and reflections from the surrounding terrain, as well as loss due to obstruction of the horizon and (3) loss due to absorption and scattering by clouds.

[37] In the next section, the effects of these processes are quantified by means of a parameterization scheme. The developed procedure derives all factors from local terrain characteristics as well as physical and empirical relations. It computes the effects of hillshading, decrease of atmospheric transmittance due to the individual processes of scattering, and considers multiple reflections between the atmosphere and the ground as well as reflections from surrounding terrain. Direct and diffuse shortwave radiative fluxes for each grid cell are parameterized after a rigorous evaluation of the DEM of the area using efficient vectorial algebra algorithms, the principles of which are described in detail by *Corripio* [2003]. First, potential direct solar radiation is determined for each grid cell. Then, slope, aspect and cell surface area are represented as a vector normal to the surface and calculated using the minimum area unit of the DEM which is enclosed between four data points. This vector is half the sum of cross products of the vectors along the sides of the grid cell. The position of the sun is calculated by applying rotational matrices to a unit vector defined at noon as a function of latitude and declination. The rotation matrix is dependent on the hour angle ω for a given latitude and declination:

$$\omega = \pi \cdot \left(\frac{t}{12} - 1\right) \tag{3}$$

with t being the local apparent time in hours and decimal fraction.

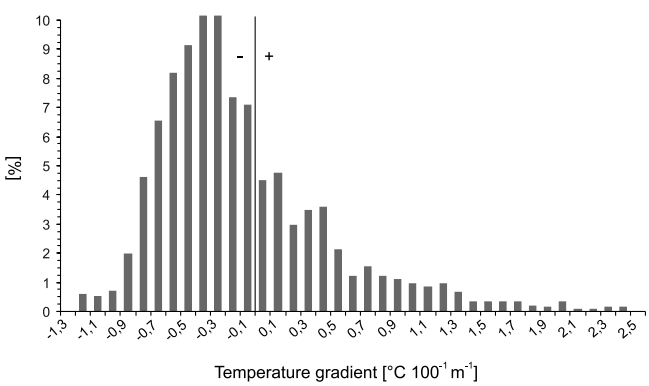

Figure 8. Percentual fraction of hourly temperature gradients between stations 1 and 5 for Haut Glacier d'Arolla.

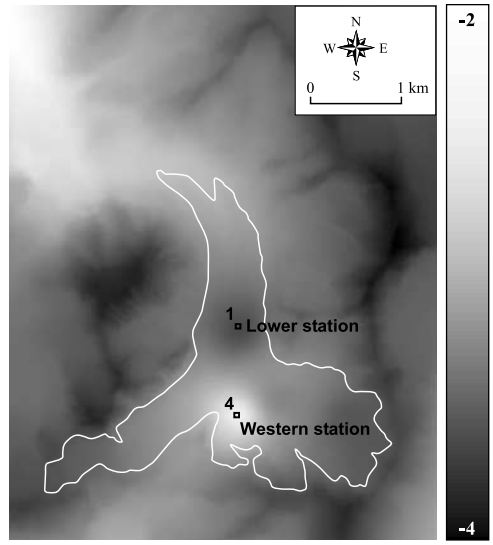

Figure 9. Interpolated temperature (°C) for Haut Glacier d'Arolla (0200 LT, 5 June 2001).

[38] The declination δ is computed after *Bourges* [1985] with a Fourier series approximation:

$$\begin{aligned}\delta = {} & 0.3732 + 23.2567 \cdot \sin(D) - 0.758 \cdot \cos(D) \\ & + 0.1149 \cdot \sin(2 \cdot D) + 0.3656 \cdot \cos(2 \cdot D) \\ & - 0.1712 \cdot \sin(3 \cdot D) + 0.0201 \cdot \cos(3 \cdot D)\end{aligned} \tag{4}$$

with D being the day number:

$$D = \left(\frac{2 \cdot \pi}{365.25}\right) \cdot (J - 79.346) \tag{5}$$

J is the Julian day, 1 on the first of January and 365 on 31 December.

[39] The direct component of insolation intercepted by each cell surface is then calculated as a dot product between the unit vector in the direction of the sun and the unit vector normal to the surface, multiplied by direct normal irradiation, i.e., the solar constant (1367 W m^{-2}) which is corrected with a multiplicative factor c for excentricity after *Spencer* [1971], Γ being the day angle ($\Gamma = \frac{2 \cdot p \cdot (J-1)}{365}$):

$$\begin{aligned}c = {} & 1.000110 + 0.034221 \cdot \cos(\Gamma) + 0.001280 \cdot \sin(\Gamma) \\ & + 0.000719 \cdot \cos(2 \cdot \Gamma) + 0.000077 \cdot \sin(2 \cdot \Gamma)\end{aligned} \tag{6}$$

Hillshading is computed by scanning the projection of cells onto a solar illumination plane perpendicular to the sun direction. By checking the projection of a grid cell over this plane, following the direction of the sun, it is determined whether a point is in the sun or in the shade of another cell. To increase computational efficiency of the algorithm, an array of cells is defined for every cell on the sun side of the grid border; the length of this array is given by the nearest intersection of a line along the vector opposite to the sun and the DEM boundaries.

[40] Horizon angles and estimated sky view factor are calculated using a more economical algorithm than a rigorous evaluation of all the angles subtended by every

grid cell to each other [*Corripio*, 2003]. The sky view factor is an important parameter for the computation of incoming diffuse and multiple scattered shortwave radiation, especially in areas of high albedo like snow covered mountains, and for the net balance of longwave radiation. Following *Iqbal*'s [1983] unit sphere method, the sky view factor is computed as the ratio of the projected surface of visible sky onto the projected surface of a sphere of unit radius [*Nunez*, 1980]. For the computation of the horizon zenith angles for selected azimuths a modification of *Corripio*'s [2003] shading algorithm is used. To save computation time, the sky view factors for all grid cells are stored in a separate file which is read in at the beginning of a simulation run.

[41] The actual direct shortwave radiation at normal incidence I is computed accounting for the total transmittance of the atmosphere, given as the product of the individual transmittances. First, an additional correction $\beta(z)$ for altitude after *Bintanja* [1996] is introduced to account for the increase of transmittance with surface height (in W m^{-2}):

$$I = 1367 \cdot c \cdot \left(\tau_r \cdot \tau_o \cdot \tau_g \cdot \tau_w \cdot \tau_a + \beta(z)\right) \tag{7}$$

with τ_r being the transmittance due to Rayleigh scattering, τ_o the transmittance by ozone, τ_g the transmittance by uniformly mixed trace gases, τ_w the transmittance by water vapour and τ_a the aerosol transmittance, all of them referring to sea level. The correction for altitude $\beta(z)$ is linear up to 3000 m a.s.l. (and kept constant for higher elevations) and is given by:

$$\beta(z) = 2.2 \cdot 10^{-2} \cdot km^{-1} \tag{8}$$

The individual transmittances are computed as follows [*Bird and Hulstrom*, 1981; *Iqbal*, 1983]. The relative optical path length m is computed after *Kasten* [1966] and corrected for altitudes other than sea level, thereby p being the local pressure in hPa and θ_z the solar zenith angle:

$$m = \left(\frac{p}{1013.25} \cdot \frac{1}{\cos\theta_z + 0.15 \cdot (93.885 - \theta_z)^{-1.253}}\right) \tag{9}$$

1013.25 is the sea level pressure in hPa. The transmittance due to Rayleigh scattering, τ_r, is given by:

$$\tau_r = e^{\left[-0.0903 \cdot m^{0.84} \cdot \left(1 + m - m^{1.01}\right)\right]} \tag{10}$$

The transmittance by ozone τ_o can be computed (with l being the vertical ozone layer thickness, assumed to be 0.35 cm according to measurements from Total Ozone Mapping Spectrometer-Earth Probe (TOMS-EP 2001, Total Ozone Mapping Spectrometer-Earth Probe data sets, http://toms.gsfc.nasa.gov/eptoms/ep.html):

$$\tau_o = 1 - \left[0.161 \cdot l \cdot m - \frac{1}{(1 + 139.48 \cdot l \cdot m)^{0.3035}} - 0.02715 \cdot l \cdot m \cdot \frac{1}{1 + 0.044 \cdot l \cdot m + 0.0003 \cdot (l \cdot m)^2}\right] \tag{11}$$

The transmittance by ozone is the only transmittance which is spatially invariant for the area. The transmittance by uniformly mixed trace gases τ_g is computed with:

$$\tau_g = e^{\left(-0.0127 \cdot m^{0.26}\right)} \tag{12}$$

τ_w, the transmittance by water vapour, is computed with w being the precipitable water in cm:

$$\tau_w = 1 - 2.4959 \cdot w \cdot m \cdot \frac{1}{(1 + 79.034 \cdot w \cdot m)^{0.6828} + 6.385 \cdot w \cdot m} \tag{13}$$

Thereby, the precipitable water is computed after *Prata* [1996] with e_0 being the actual vapour pressure at the site and T_a the air temperature in K:

$$w = 46.5 \cdot \frac{e_0}{T_a} \tag{14}$$

Finally, the aerosol transmittance τ_a is calculated as follows, v being the (prescribed) visibility in km:

$$\tau_a = \left(0.97 - 1.265 \cdot v^{-0.66}\right)^{m^{0.9}} \tag{15}$$

For the computation of the diffuse component of shortwave radiative fluxes the following processes are taken into account: Rayleigh and aerosol scattering, multiple reflections between the atmosphere and the ground as well as reflections from the surrounding terrain. The transmittance due to Rayleigh scattering, τ_{rr}, is given with

$$\tau_{rr} = \frac{0.395 \cdot \cos(\theta_z) \cdot \tau_o \cdot \tau_g \cdot \tau_w \cdot \tau_{aa} \cdot (1 - \tau_r)}{(1 - m + m^{1.02})} \tag{16}$$

with τ_{aa} being the transmittance of scattered direct radiation due to aerosol absorptance, computed using $\omega_0 = 0.9$ as assumed single scattering albedo:

$$\tau_{aa} = 1 - (1 - \omega_0) \cdot \left(1 - m + m^{1.06}\right) \cdot (1 - \tau_a) \tag{17}$$

Transmittance due to aerosol scattering, τ_{as}, is given with

$$\tau_{as} = \frac{\cos(\theta_z) \cdot \tau_o \cdot \tau_g \cdot \tau_w \cdot \tau_{aa} \cdot F_c \cdot \left(1 - \frac{\tau_a}{\tau_{aa}}\right)}{(1 - m + m^{1.02})} \tag{18}$$

F_c is the ratio of forward scattering to total scattering. It is computed as regression from the tabulated values given by *Robinson* [1966] as:

$$F_c = 0.9067 + 0.1409 \cdot \theta_z - 0.2562 \cdot \theta_z^2 \tag{19}$$

Now, the effect of multiple reflections between the atmosphere and the ground is calculated. Therefore the sum of the radiative fluxes as computed with equations (7) to (19) is increased by a factor m_r which is given by:

$$m_r = \frac{a_g \cdot a_a}{1 - a_g \cdot a_a} \tag{20}$$

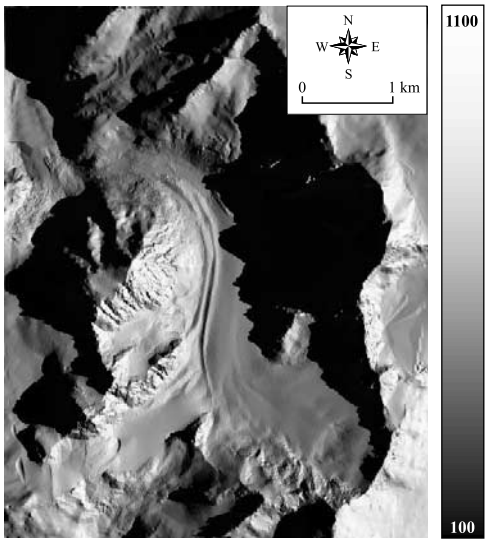

Figure 10. Simulated shortwave radiative fluxes (W m$-^2$) for Haut Glacier d'Arolla (0900 LT, 1 June 2001).

a_a is the atmospheric albedo, computed as:

$$a_a = 0.0685 + (1 - F_c) \cdot \left(1 - \frac{\tau_a}{\tau_{aa}}\right) \tag{21}$$

0.0685 is the assumed clear sky albedo. Since slopes not visible from the site, but located in its vicinity, contribute to diffuse radiative fluxes by multiple scattering, ground albedo a_g is assumed to be the mean albedo of the DEM area. It is computed as the area weighted sum of rock albedo (assumed to be 0.15, corresponding to mean observed albedos of gneiss and granite), ice albedo (assumed to be 0.10, according to the observations) and snow albedo (parameterized as described later in the albedo section).

[42] For the estimation of the area fraction of the different surface types we applied a temperature index snowmelt model considering simulated (clear sky) solar radiation G^* and parameterized albedo α, M being the hourly melt rate in mm [*Pellicciotti et al.*, 2003]:

$$M = \frac{1}{24} \cdot tf \cdot T_a + af \cdot G^* \cdot (1 - \alpha) \quad \text{for} \quad T_a > 1°C \tag{22}$$

tf and af are empirical coefficients, called temperature and albedo factor, respectively, expressed in mm d^{-1} °C^{-1} and m^2 mm h^{-1} W^{-1}. Calibration with melt rates computed for the central site with an energy balance model [*Brock and Arnold*, 1985] led to $tf = 0.05$ mm h^{-1} °C^{-1} and $af = 0.0094$ m^2 mm h^{-1} W^{-1}. The initial snow water equivalent distribution was derived from interpolated measurements taken in the beginning of the melt season, applying the interpolation procedure as described above.

[43] Finally, the sum of the direct and diffuse radiative fluxes are corrected for the visible portion of the hemisphere by multiplying their sum with the sky view factor for each pixel. In a last step, direct reflections from the surrounding terrain are added by considering the shortwave radiation, the ground view factor and the fraction as well as albedo of the reflecting surfaces.

[44] The presented solar radiation model is parametric and not truly physical. Nevertheless, it gives good estimates of the individual atmospheric transmittances [*Niemelä et al.*, 2001] and can be applied for any area if an appropriate DEM is available. Figure 10 shows the result of the described computation of the shortwave radiative fluxes for a single time step at Haut Glacier d'Arolla. Comparison with the measurements for clear sky conditions at the locations of Stations 0 and 2 resulted in good agreement for a wide range of conditions (Figure 11).

[45] As a result of the described procedure, the mean effects of the mentioned processes on the extraterrestrial flux can be quantified (Figure 12). For all stations, the gain of energy is mainly due to terrain reflections and multiple reflections. On the average, this combined effect accounts for 10.6% of energy gain related to the extraterrestrial flux, being most efficient in areas with steep slopes around (Stations 0 and 4). On the other hand, horizon obstruction and thus related loss of energy is also largest for Stations 0 and 4 (12.0%), which are situated in a narrow, east-west oriented valley with a high mountain southward, and at the foot of a steep, north facing slope, respectively. Horizon obstruction is less for Stations 2 and 3 which were installed in the open upper se basin of the glacier (9.0%). The effects of Rayleigh and aerosol scattering and absorption by water vapour, ozone and other trace gases are all comparably homogeneous in the area and reduce the energy of the extraterrestrial flux by 5.4%, 2.2%, 1.3%, 10.0% and 7.9%.

[46] Of all factors affecting shortwave radiation the cloud factor is the most effective. Its mean value was computed by the ratio of the total measured shortwave radiation to the total computed clear sky radiation for the period 1 to 21 June and 18 July to 31 August. Therefore the cloud factor includes not only the direct effect of the clouds on the shortwave radiation but also the intensification of multiple scattering. On average, clouds account for 30.0% of loss of energy of the extraterrestrial flux. The local variations of the cloud factor should be interpreted with caution, since, being indirectly derived, it integrates all measurement errors and parameterization uncertainties. For Station 0, e.g., the western horizon (with Pigne d'Arolla, 3796 m a.s.l.) is not within the DEM area and so the computed horizon obstruction, derived from the DEM for the location of this station,

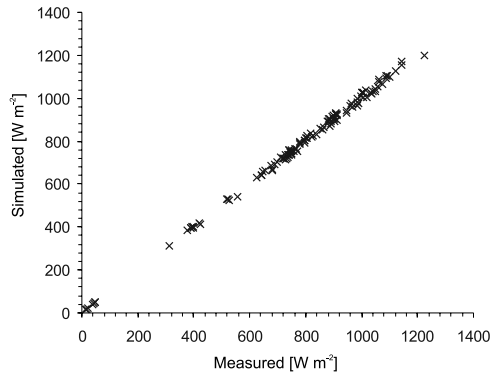

Figure 11. Measured versus simulated shortwave radiative fluxes for clear sky conditions at Haut Glacier d'Arolla, melting period of summer 2001, for the locations of Stations 0 and 2. n = 122, R^2 = 0.998.

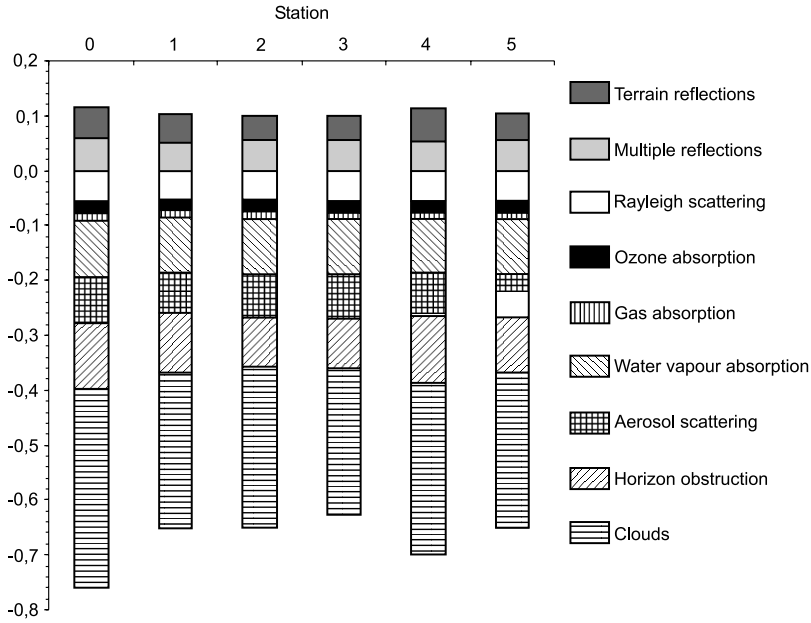

Figure 12. Gain and loss of energy due to different processes affecting the shortwave radiation fluxes, scaled by the extraterrestrial flux, at Haut Glacier d'Arolla. Ozone absorption is spatially constant.

is too small by an unknown extent. However, contributions from low angular elevations make only minor contributions to total hemispheric irradiance of a horizontal surface. Other simplifications for the estimation of the attenuation of the shortwave radiative fluxes include prescribed model parameters (e.g., vertical ozone layer thickness or visibility) or mean estimates like the albedo of rock ground which was preset to 0.15 according to our observations.

[47] On the average for all stations, potential shortwave radiation is reduced by an amount of 57%, considerably more than on the Pasterze Glacier as found by *Greuell et al.* [1997]. The difference is mainly due to the effect of clouds, i.e., the specific meteorological conditions during our experiment, and the larger horizon obstruction at Haut Glacier d'Arolla.

3.5. Albedo

[48] The albedo of the glacier surface depends on many factors: whether the surface is snow or ice, the amount of debris cover on the ice and the grain size, water, and impurity content of snow. The reflectivity of snow and ice is also dependent on wavelength, normally decreasing from the visible to the near infrared. It was measured at all locations using albedometers which consist of two opposed pyranometers facing up and down. To avoid geometrical errors, measurements were made in a surface parallel plane [*Mannstein*, 1985]. Daily values for all the stations are plotted in Figure 13, whereby 11:30 local time recordings were chosen to be representative for the day (10:00 UTC), since albedo increases at higher zenith angles and cloudiness, and the latter is more probable to occur in the afternoon. The glacier surface at Stations 4 and 5 in the upper basin was snow covered during the entire period of the experiment. At the other stations on the glacier, the snow disappeared during August and bare ice became exposed, the albedo of which was 0.1 to 0.2, mainly depending on the moraine material content on the surface (Station 1 was set up on the medial moraine). The glacier foreland at Station 0 became snowfree earlier, during June. There, rocks with sparse pioneer vegetation became exposed. The albedo of this type of ground was measured to be 0.15.

[49] On the glacier, the observed decrease of the surface albedo with time due to the ageing of the snow is typical. Its course is interrupted by superimposed peaks caused by fresh snowfalls. On 28 June snowfall occurred on the glacier and thus increased the surface albedo, but rainfall occurred in the valley below the glacier, where it reduced the snow albedo. The sharp decline of albedo with the disappearance of the snow cover is a crucial turning point in energy balance considerations: energy absorption of the glacier is then enhanced by almost 50%.

[50] For an examination of albedo over the entire glacier area, a Landsat 7 ETM+ scene of 30 July 2001 was processed. Radiometric correction was calculated using the ATCOR3 algorithm [*Richter*, 2001] which is based on lookup tables computed with the MODTRAN 4 radiative transfer code [*Berk et al.*, 1999]. Geometric correction, including a surface topography correction, was conducted employing the DEM of the area with 10 m resolution. Broadband surface albedo α was then derived from the corrected images of TM bands 2 and 4 using the following empirical relation [*Knap et al.*, 1999a]:

$$\alpha = 0.726 \cdot \alpha_2 - 0.322 \cdot \alpha_2^2 - 0.051 \cdot \alpha_4 + 0.581 \cdot \alpha_4^2 \qquad (23)$$

with α_2 and α_4 being the narrowband corrected surface reflectances of TM bands 2 (0.52 to 0.60 μm) and 4 (0.76 to 0.90 μm), respectively. Equation (23) was developed for a representative set of glacier surface types ranging from completely debris covered glacier ice to dry snow on the Morteratschgletscher in Switzerland. *Knap et al.* [1999b] showed that equation (23) is the most accurate relation available.

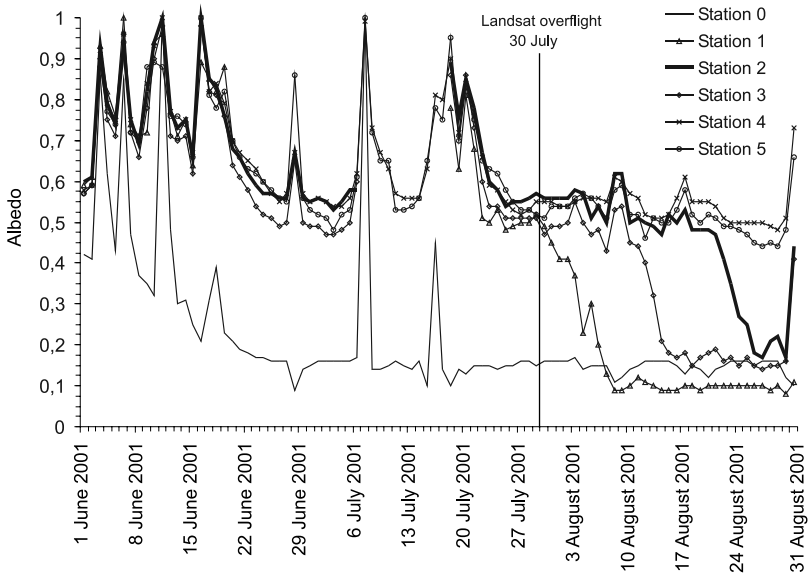

Figure 13. Measured daily surface albedo for the locations of the meteorological stations at Haut Glacier d'Arolla.

[51] On 30 July, the lower part of the glacier tongue was already snowfree (Figure 14): there, areas with moraine material (i.e., lower albedo) can be distinguished from clean ice. In the photograph, taken at almost the same time, the medial moraine is clearly visible. In the transition zone between ice and snow intermediate albedo values of approximately 0.3 can be detected, according to old snow contaminated with moraine dust and slush. The troughs on both sides of the western lateral moraine are still full with snow, as can be seen from both the satellite data and the photograph.

[52] On 30 July all five AWSs were still on snow and there was very little spatial variation in albedo recorded, with measured values ranging from 0.48 (Station 3) to 0.55 (Station 2). These albedo values are typical of old snow which has undergone several days or more of melting. Such low spatial variability of albedo across old snow surfaces at Haut Glacier d'Arolla was also reported by *Brock et al.* [2000b].

[53] Figure 15 shows the fractional distribution of albedo values at the glacier surface at the Landsat overpass as derived from the satellite data. In 34.5% of the glacier surface area the albedo is between 0.26 and 0.48, almost homogeneously distributed, representing the various surface types of bare glacier ice with moraine material and dirty slush. 64% of the glacier area are still covered with snow

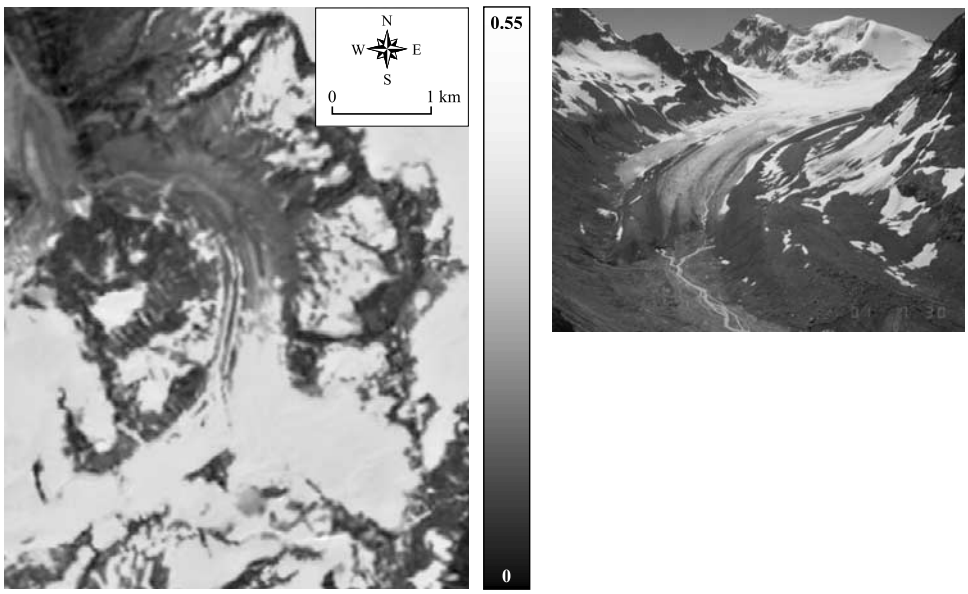

Figure 14. Surface albedo at Haut Glacier d'Arolla derived from Landsat-7 ETM + 195/28, 1030 UTC, 30 July 2001 (left) and terrestrial photograph of the tongue and central area of the glacier at 1100 UTC of the same day (right). Viewing direction of the photograph is south.

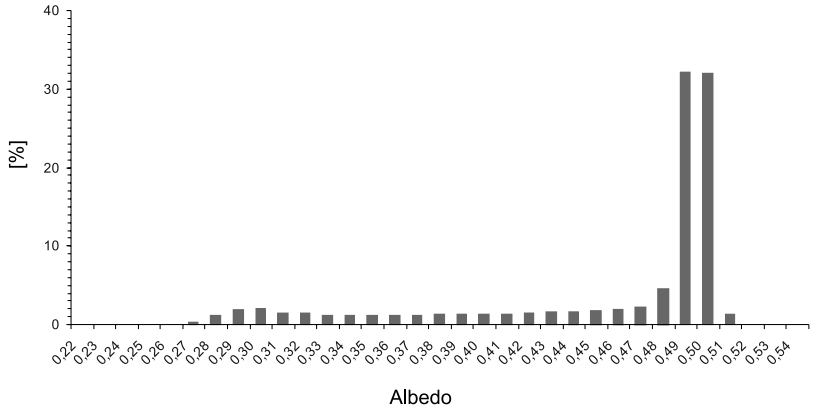

Figure 15. Area fraction of surface albedo values as derived from Landsat TM satellite data for Haut Glacier d'Arolla, 30 July 2001.

with albedo of 0.49 and 0.50, and only in 1.5% of the area the albedo is higher than that (0.51 to 0.54). The pixels belonging to the latter class are randomly distributed in space in the upper basin of the glacier. The homogeneity of the albedo on the old snowpack is striking, while the absence of albedos higher than 0.54 indicates that significant melting was occurring at all elevations.

[54] Satellite images of appropriate temporal and spatial resolution, from which albedo can be derived for continuous, distributed glacier melt modeling, are commonly not available. Normally, parameterizations have to be used, mostly employing the age of the snow surface as a surrogate for the processes which have an effect on albedo. To compare the parameterized albedo with the measurements and the satellite data derived albedo we modelled the snow albedo a using the ageing curve approach [*U.S. Army Corps of Engineers*, 1956]:

$$a = a_{min} + a_{add} \cdot \mathrm{e}^{-kn} \tag{24}$$

where k is a recession factor depending on the snow surface temperature and n the number of days since the last considerable snowfall which causes an increase of the snow albedo to its maximum value. This function has proven its reliability in many larger-scale applications [e.g., *Strasser and Mauser*, 2001; *Schulla*, 1997; *Plüss and Mazzoni*, 1994].

[55] The k factors in (24) were optimized with measurements by means of a Monte Carlo simulation: efficiencies were calculated using equation (24) for the ranges of k factors as given in Figure 16. For the simulation at Haut Glacier d'Arolla, averages in the optimum space for the two stations were found at k = 0.3 (negative temperatures) and k = 0.4 (positive temperatures). a_{min} was set to 0.5, and a_{add} was set to 0.45 by visual analysis of the measurements (see Figure 13).

[56] With equation (24), albedo is simulated on a daily basis, using the independent variables time and air temperature which correlate well with long term changes to the reflectance properties of the glacier surface associated with snow metamorphism and the build up of light absorbing impurities. Therefore temperature and precipitation fields (as provided with the interpolation scheme as described above) are aggregated to daily fields by summing and averaging, respectively. A daily snowfall of more than 1 mm water equivalent is interpreted as significant, i.e., then albedo is reset to its maximum value of 0.95. A temperature of 1°C was set to be the threshold for the

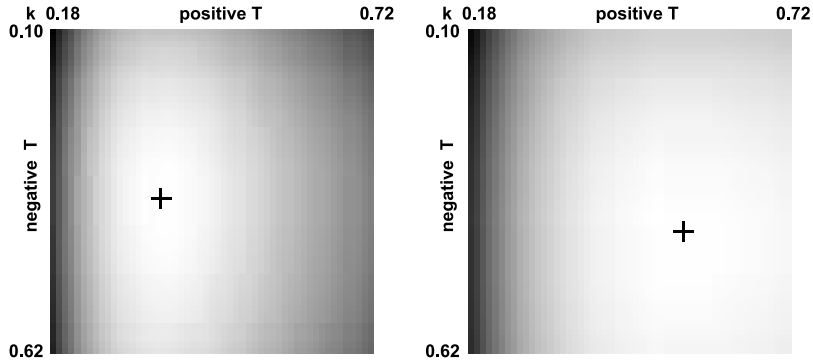

Figure 16. Monte Carlo simulation for the determination of optimal recession factors for negative (vertical axes) and positive (horizontal axes) mean daily 2 m air temperatures. Left: Station 4, right: Station 5, Haut Glacier d'Arolla, 1 June to 31 August 2001. Brighter areas represent higher efficiencies for the k combinations in the albedo parameterization. The crosses mark the position of the maximum efficiencies achieved: R^2 = 0.60 (Station 4) and R^2 = 0.49 (station 5).

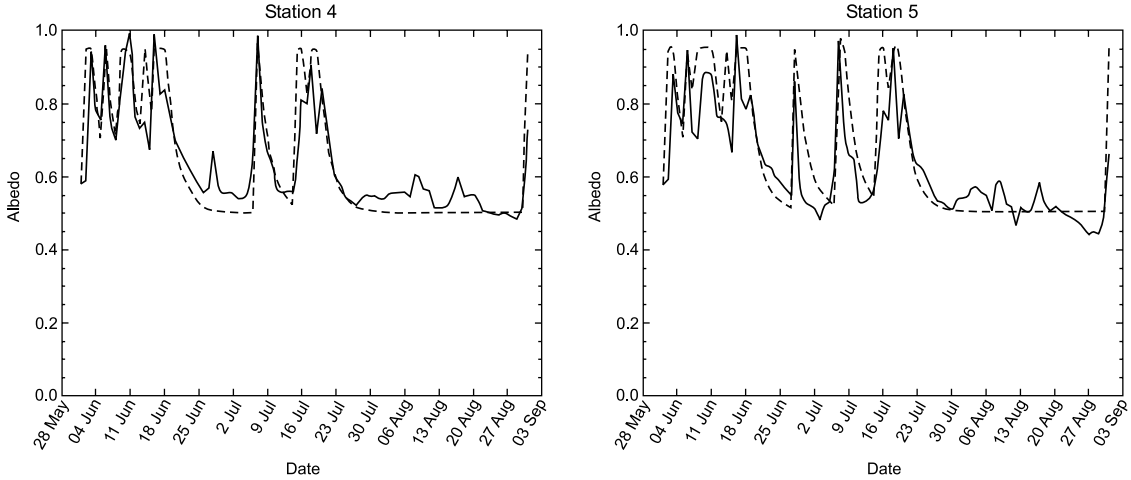

Figure 17. Comparison beween parameterized (dashed line) and measured (solid line) albedo for stations 4 (left) and 5 (right) at Haut Glacier d'Arolla.

phase change between snow and rain. In Figure 17, the simulated course of albedo is shown in comparison with the station measurements: June is characterized by a series of fresh snow falls with interrupted ageing and corresponding resets of albedo. The event of 28 June was a significant snowfall event at Station 5 and correctly simulated as such. At Station 4, however, it was warmer, and less precipitation fell as snow, as visible in the measurement and the simulation (no albedo reset). The two events in July are both represented well by the simulation, as is the first snowfall in autumn at the end of August. The intermediate measured changes of old snow albedo in between, not reproduced by the parameterization, can be due to rainfall events, melting and refreezing, metamorphosis, rime and dust on the surface, changes of cloudiness, etc.

[57] In Figure 18, values are compared for the albedo as measured, parameterized and derived from the satellite data. The parameterized and satellite derived albedos are similar, but constant for all five station locations (0.51 and 0.49). Thus deviations between the data are ranging between 0.0 (measured/Landsat at Station 1) to 0.06 (measured/Landsat at Station 2), the latter corresponding to 11.4%. This deviation might be attributable to all three of the procedures, the measurement technique, the parameterization scheme and the satellite data processing as well. Small differences between the measured and satellite derived albedos are not surprising, however, given the AWSs sample a much smaller area of the glacier than a satellite pixel. For a measurement height of 2 m, 90% of the radiation received by the down-facing pyranometer is received from an area of the glacier surface of approximately 113 m^2 (following *Schwertfeger* [1976]), whereas a Landsat TM pixel has a ground area of 900 m^2.

[58] Our hourly time series of glacier albedo measurements not only display significant variability at long (> day), but also at short (< day) timescales. These short term albedo variations are mainly attributable to changes in illumination conditions caused by variations in cloud cover and solar zenith angle. We made an attempt to assess how significant such short term albedo variations are to estimate the errors which may result from using a constant daily albedo (e.g., to calculate surface melt rates). Comparison between daily net shortwave radiation flux calculated from measured incoming and outgoing fluxes and the net shortwave radiation flux calculated from the measured incoming flux and a constant average daily albedo showed only small differences. This is because, while increases in cloud cover and solar zenith angle cause the albedo to increase, the incoming shortwave flux decreases under these same conditions.

3.6. Longwave Radiation

[59] The mean measured incoming longwave radiative flux at Station 0 and 2 is 294 and 279 W m^{-2}, respectively (see Table 3). The difference can be attributed to three main phenomena: (1) differences in air temperature and its vertical profile (2) differences in effect of upper hemisphere slopes and (3) differences in the effect of clouds. These phenomena will be discussed and quantified by means of a parameterization scheme in the following. It should always be kept in mind that Station 0 is situated in the valley on icefree ground below the glacier, whereas Station 2 on the glacier remained on snow (later ice) during the entire period of the experiment. To examine the causal differences we

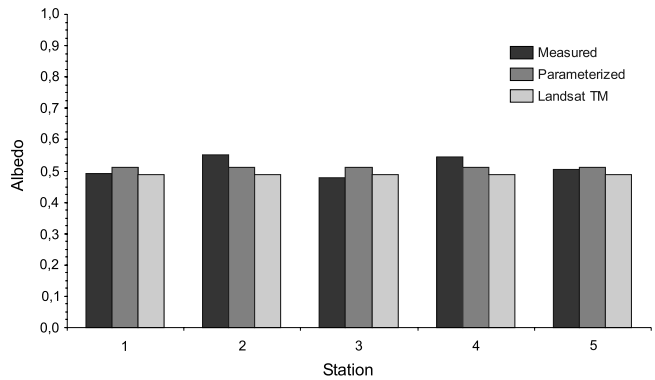

Figure 18. Albedo as measured, parameterized and derived from Landsat TM satellite data for the locations of the five meteorological stations at Haut Glacier d'Arolla, 30 July 2001.

compared the simulated longwave fluxes for different topographic and atmospheric conditions (Figure 19).

[60] The most obvious reason for the higher incoming longwave radiative fluxes at Station 0 is that the mean 2 m measured temperature was more than 3°C higher than at Station 2, due to the difference in elevation of approximately 400 m between the two stations. However, most longwave radiation reaching the surface is emitted from the lowest layers of the atmosphere which are not necessarily correctly represented by measurements of temperature at the 2 m level. Therefore depending on the height of the inversion layer, the longwave radiative flux emitted can be larger at one location than at the other due to a different temperature profile. To quantify this effect, clear sky situations were selected from the data of Stations 0 and 2 by defining a cloud factor threshold of 0.975, resulting in a subset of respectively 201 and 273 hourly records. The cloud factor is computed as the ratio of measured to computed clear sky shortwave radiation for the time step. For these situations, and without consideration of the effect of upper hemisphere slopes, the difference of mean incoming longwave radiative fluxes due to temperature and its profile is 13 W m^{-2}.

[61] Next, the effect of upper hemisphere slopes on the longwave radiative fluxes is taken into account. The upper hemisphere field of view (FOV) of Station 0 has a larger portion of upper hemisphere slopes (12%) than that of Station 2 (9%), enhancing the increase of longwave radiative fluxes at Station 0, since radiances received from slopes are larger than the ones received from the sky. Furthermore, at Station 0 the surrounding slopes are generally more snowfree than around the central area of the glacier, and snowfree slopes are likely to have higher mean surface temperatures than slopes covered by snow.

[62] The incoming longwave radiative flux from surrounding slopes consists of a fraction emitted by rocks, and a remaining part emitted by snow. The temperature T_r of the emitting rocks is set equal to the air temperature during nighttime, but during daytime it is higher than the air temperature by an amount T_+ which is dependent on the amount of the incoming shortwave radiation G (in W m^{-2}):

$$T_+ = j \cdot G \tag{25}$$

Therefore *Greuell et al.* [1997] determined j from measurements of slope temperature by means of a Heymann IR sensor. Relating these measurements to simultaneous values of the global radiation yielded $j = 0.01$°C m^2 W^{-1}, meaning that during maximum insolation conditions (~1000 W m^{-2}) the mean temperature of those parts of the slopes not covered by ice or snow is 10°C higher than the temperature above the glacier. For the fraction of surrounding slopes which is covered by snow, the temperature is set equal to T_a, but cannot exceed 0°C. Whether a cell is snow covered or not is determined hourly with the temperature index melt model considering simulated (clear sky) solar radiation and parameterized albedo (equation (22)). The effects of the atmosphere and of clouds between the surrounding slopes and the cell under consideration are neglected.

[63] Taking into account the effect of the surrounding slopes with the described procedure leads to an increase of longwave radiative fluxes of 40 W m^{-2} (Station 0) and 30 W m^{-2} (Station 2). Now, considering both the effects of temperature and its profile as well as upper hemisphere slopes, the difference of mean incoming longwave radiative fluxes between Station 0 and 2 is 23 W m^{-2}.

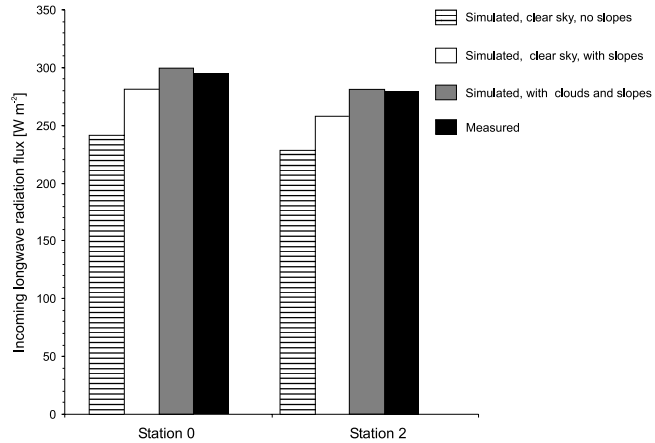

Figure 19. Mean incoming longwave radiative fluxes for stations 0 and 2 at Haut Glacier d'Arolla.

[64] Up to now, all simulations do not consider the effect of clouds, which in principle enhance the incoming longwave radiative flux due to their water content. Since observations of the cloud amount are not available, cloudiness C is derived from the cloud factor cF by inverting the fit function found by *Greuell et al.* [1997] for the Pasterze Glacier area. *Greuell et al.* [1997] concluded that their data is in line with monthly values for the cloud factor for different elevations based on data from Austrian climate stations published by *Sauberer* [1955]. Here, it is assumed that the relation is also valid for Haut Glacier d'Arolla:

$$C = 0.997 + 0.4473 \cdot cF - 1.4059 \cdot cF^2 \tag{26}$$

According to the Stefan Boltzmann law, the incoming longwave radiative flux from the sky is estimated by the Stefan Boltzmann constant, the fourth power of the air temperature and the emissivity of the sky; then it is further modified by the skyview factor. Thereby, the emissivity of the sky ε is computed as:

$$\varepsilon = \varepsilon_{cs} \cdot \left(1 - C^2\right) + \varepsilon_{oc} \cdot C^2 \tag{27}$$

ε_{oc}, the emissivity of totally overcast skies, is assumed to be 0.976 (after *Greuell et al.* [1997]). ε_{cs}, the emissivity of the clear sky, is computed after *Prata* [1996]:

$$\varepsilon_{cs} = 1 - (1 + w) \cdot e^{-\sqrt{(1.2+3 \cdot w)}} \tag{28}$$

Simulating the effect of the clouds using equations (26) and (27) leads to an increase of the longwave radiative fluxes of 18 W m^{-2} (Station 0) and 22 W m^{-2} (Station 2), respectively, i.e., the effects of temperature and slopes are compensated for a little. Finally it can be concluded that the difference of mean incoming longwave radiative fluxes between the two stations, according to the simulations, is

19 W m^{-2}, whereas the measured one is 15 W m^{-2} (see Table 3), showing that the parameterization is reliable.

4. Conclusions

[65] In this paper three months of measurements taken at six meteorological stations on and in front of Haut Glacier d'Arolla (Switzerland) during the 2001 ablation season are discussed. The main focus of interest is the temporal and spatial variability of the observations, as well as a quantitative discussion of the observed patterns by means of parameterization techniques. The comparison of the results with those of the only other comparable study of spatial variations of meteorological variables on an alpine glacier [*Greuell et al.*, 1997] can be useful as a reference for future studies of glacier-climate relations and meteorological variability in mountain regions.

[66] The wind regime on the glacier was dominated by the glacier wind. Only at high wind speeds, corresponding with strong northwesterly air flows, did the main wind direction change from the glacier wind to the synoptic gradient wind direction. In contrast to the Pasterze Glacier these two directions are directly opposed, thus mean directional constancies are much lower on Haut Glacier d'Arolla, ranging from 0.15 to 0.49. Here the downvalley directivities also became negative on some days, and then the resulting mean daily wind vector had an upvalley component. Mean wind speed hardly varied with elevation and was about 2.8 m s^{-1}, considerably less than at the Pasterze (4 m s^{-1}), as would be expected on a smaller glacier with smaller katabatic forcing. For both sites, the glacier wind speed did not increase with 2 m temperature, despite the potential for increased katabatic forcing. The wind speed frequency distribution was found to be positively skewed for all stations, and the variability of the functions was considerably less than at the Pasterze. Such distribution functions can be used to impose random variations to the usually prescribed wind speed (constant with elevation and in time), leading to an improvement in the consideration of the turbulent fluxes which are non linear in the wind speed.

[67] For the mean 2 m temperatures, a slight linear decrease with elevation was found in the data, with a mean temperature gradient of $-0.002°C\ m^{-1}$, in contrast to the results for the Pasterze, where the distribution of mean temperatures is best described by a linear relation between potential temperature and the distance along the flowline. Nevertheless, even at Haut Glacier d'Arolla the gradient was positive in 28% of the recordings, meaning that temperature increased with elevation. To preserve the temporal variations of the gradient, the described interpolation scheme can be applied if at least two stations recording temperature are available. At the two stations close to the glacier margins mean 2 m temperatures are higher than on the glacier center flow line due to the less pronounced katabatic forces. The cooling effect of a melting surface is indicated by the considerably lower mean 2 m temperatures on the glacier compared to data from adjacent operational weather stations of even higher altitude.

[68] Relative humidity was almost constant during the observational period, with a mean of 71%, similar to what was observed at the Pasterze Glacier. Temporally, short term variations of relative humidity due to specific meteorological situations are of much larger significance: the extreme values recorded are 9% and 100%, respectively.

[69] Mean shortwave radiation generally increased with elevation, although at Station 4 a local minimum was observed due to its location on an obstructed, north-facing slope. The different fluxes of shortwave radiation were separated by means of a parameterization scheme quantifying the effects of the different relevant processes. It can be concluded that spatial variations of the energy gain or loss are mainly due to horizon obstruction (loss) and reflections from surrounding slopes (gain). These effects are related to local relief and albedo. The effects of the individual scattering processes only show little spatial variation, the ozone transmissivity being spatially constant. By far the largest attenuation of shortwave radiation was due to the effect of clouds, on the average accounting for 30% of loss of energy of the extraterrestrial flux. Total attenuation of shortwave radiation accounts for 57%, considerably more than at the Pasterze Glacier, due to the more pronounced effects of clouds and surrounding topography.

[70] Mean albedo generally increased with elevation. The upper basin was snow covered during the entire period of our experiment. At the lower glacier, measured ice albedos ranged between 0.1 and 0.2 depending on moraine impurity content and liquid water on the surface. The ground albedo as recorded by the station in the glacier foreland is within the same range: these two surface types are hard to distinguish in satellite images. In the Landsat TM satellite data of 30 July, in areas of glacier ice, dirty slush and moraine the albedo varies between 0.26 and 0.48, whereas values of 0.49 to 0.52 are typical for the snow covered areas. The decrease of albedo after snowfall events showed typical trends. For old snow, during the late ablation season, almost no spatial variation of albedo could be found; neither in the measurements, nor in the data derived from the satellite image. The presented parameterization scheme, based on the ageing curve approach, represents well the measurements and can be applied if satellite data are not available with appropriate temporal resolution.

[71] Mean measured longwave radiative fluxes decreased with elevation (15 W m^{-2} less at the higher station), due to a 3°C higher mean atmospheric temperature at the lower station and the effect of upper hemisphere slopes. Again, the causes for the difference were quantified by means of parameterization of the related processes. Without clouds, the difference in longwave incoming radiative fluxes would be even more pronounced (23 W m^{-2}). The effects of the different processes affecting longwave radiation are comparable with the ones found for the Pasterze Glacier.

[72] Measurements taken at Station 4, which was atypical being situated at the foot of a large and steep glacier slope, show how much spatial variation in meteorological variables one can expect compared to the corresponding recordings of a station which is at a typical measurement site, like the central Station 2. This finding mainly accounts for wind direction, temperature, humidity and shortwave radiative fluxes.

[73] The distribution of meteorological variables on an alpine glacier and the presented parameterization techniques are a first step toward continuous distributed modeling of glacier energy and mass balances, especially their temporal and spatial variabilities. Such models are a prerequisite for

studying the climate change impact on the dynamics of the glacier behaviour and thus the effect on water resources and, ultimately, landscape evolution.

[74] Only limited conclusions are possible regarding the general validity of the distributions and parameterizations presented here. The comparison of the results with the ones derived for the Pasterze shows some similarities, but also discrepancies not attributable to local or temporal conditions alone. Further research on other glaciers will help to bridge the gaps.

Appendix A: AMUNDSEN: A Software Tool for Providing Distributed Fields of Meteorological Variables, Parameterizations, and Simulations

[75] The algorithms as described in this paper are all integrated into a new scientific software tool, Alpine Multiscale Numerical Simulation Engine (AMUNDSEN), which provides time series of spatially variable fields employing a wide range of interpolation, parameterization and simulation procedures. Basic considerations for the design of the program were: full representation of temporal and spatial variabilities, a simple interface to plug in existing models, raster and vector data capability, real-time visualization of the computed fields (i.e., during simulation) and platform independence. AMUNDSEN is coded in IDL, a programming environment which enables a very efficient coding of vector and array manipulations and which offers a large variety of pre- and postprocessing as well as visualization possibilities. IDL runs on UNIX/LINUX, Windows and Macintosh and can call external FORTRAN or C routines. In the current version, the functionality of AMUNDSEN includes several interpolation routines for scattered meteorological measurements, rapid computation of topographic parameters from a digital terrain model, parameterization of snow albedo, sophisticated simulation of short- and longwave radiative fluxes, modeling of snow- and icemelt and more. Potential applications of the program cover the simulation of physical processes in glaciology, hydrology, climatology and other alpine research fields. The code is continuously updated and available from the authors at no charge (u.strasser@iggf.geo.uni-muenchen.de).

[76] **Acknowledgments.** We are thankful to all who provided their help and assistance for writing the manuscript of this paper, in particular Wouter Greuell (Utrecht) and Wouter Knap (De Bilt) for their advices, Tobias Kellenberger and Fabiola Bigler for processing the Landsat TM data, and Herrmann Bösch who processed the digital terrain data. We also acknowledge the contributions of René Weber, Thomy Keller, Thomas Wyder and other colleagues (all Zurich) for their technical support for the field campaign. The undergraduate students Alice Pennington, Ed Blanchard (both Cambridge) and Ben Barrett (Seattle) helped on the glacier. Karl Schroff, Hilmar Ingensand (both Zurich), Martin Kaspar (Olten) and Ian Willis (Cambridge) provided expertise and instruments. Grande Dixence SA (Arolla) supported us with data and logistical cooperation, and MeteoSwiss made meteorological observations available. Vera Falck and Christian Michelbach improved the figures, and Wolfram Mauser (all Munich) generously subsidized the publication of this paper. This work was supported by ETH Zurich under internal grant. 6/98 3 and a travel grant to B. Brock from the Carnegie Trust for the Universities of Scotland.

References

Ångström, A. (1916), Über die Gegenstrahlung der Atmosphäre, *Meteorolog. Zeitschr.*, *33*, 529–538.

Arnold, N. S., I. C. Willis, M. J. Sharp, K. S. Richards, and W. J. Lawson (1996), A distributed surface energy-balance model for a small valley glacier, I, Development and testing for Haut Glacier d'Arolla, Valais, Switzerland, *J. Glaciol.*, *42*(140), 77–89.

Berk, A., et al. (1999), MODTRAN4 Radiative Transfer Modeling For Atmospheric Correction, *Airborne Visible/Infrared Imaging Spectrometer (AVIRIS) 1999 Workshop Proceedings*, Jet Propuls. Lab., Pasadena, Calif.

Bintanja, R. (1996), The parameterization of shortwave and longwave radiative fluxes for use in zonally averaged climate models, *J. Clim.*, *9*, 439–454.

Bird, R. E., and R. L. Hulstrom (1981), A simplified clear sky model for direct and diffuse insolation on horizontal surfaces, *Tech. Rep. SERI/TR-642-761*, Sol. Res. Inst., Golden, Colo.

Blöschl, G. (1999), Scaling issues in snow hydrology, *Hydrol. Processes*, *13*, 2149–2175.

Bolz, H. (1999), Die Abhängigkeit der infraroten Gegenstrahlung von der Bewölkung, *Z. f. Meteorol.*, *3*, 97–100.

Bourges, B. (1985), Improvement in solar declination computation, *Sol. Energy*, *35*, 367–369.

Brock, B. W., and N. S. Arnold (1985), A spreadsheet-based (Microsoft Excel) point surface energy balance model for glacier and snow melt studies, *Earth Surf. Processes Landforms*, *25*, 649–658.

Brock, B. W., I. C. Willis, M. J. Sharp, and N. S. Arnold (2000a), Modelling seasonal and spatial variations in the surface energy balance of Haut Glacier d'Arolla, Switzerland, *Ann. Glaciol.*, *31*, 53–62.

Brock, B. W., I. C. Willis, and M. J. Sharp (2000b), Measurement and parameterisation of albedo variations at Haut Glacier d'Arolla, Switzerland, *J. Glaciol.*, *46*(155), 675–688.

Brunt, D. (1932), Notes on radiation in the atmosphere, I. *Q. J. R. Meteorol. Soc.*, *58*, 389–420.

Brutsaert, W. (1975), On a derivable formula for long-wave radiation from clear skies, *Water Resour. Res.*, *11*, 742–744.

Corripio, J. (2003), Vectorial algebra algorithms for calculating terrain parameters from DEMs and solar radiation modelling in mountainous terrain, *Int. J. Geogr. Inf. Sci.*, *17*(1), 1–23.

Escher-Vetter, H. (2000), Modelling meltwater production with a distributed energy balance method and runoff using a linear reservoir approach-results from Vernagtferner, Oetztal Alps, for the ablation seasons 1992 to 1995, *Z. Gletscherkd. Glazialgeol.*, *36*(1), 19–50.

Garnier, B., and A. Ohmura (1968), A method of calculating the direct shortwave radiation income on slopes, *J. Appl. Meteorol.*, *7*, 796–800.

Greuell, W., and R. Böhm (1998), 2 m temperatures along melting mid-latitude glaciers, and implications for the sensitivity of the mass balance to variations in temperature, *J. Glaciol.*, *44*(146), 9–20.

Greuell, W., and P. Smeets (2001), Variations with elevation in the surface energy balance on the Pasterze (Austria), *J. Geophys. Res.*, *106*, 31,717–31,727.

Greuell, W., W. Knap, and P. Smeets (1997), Elevational changes in meteorological variables along a midlatitude glacier during summer, *J. Geophys. Res.*, *102*, 25,941–25,954.

Hock, R. (1998), Modelling glacier melt and discharge (Zür. Geogr. Schriften 70), 126 pp., Dept. of Geography, ETH Zurich, Zurich, Switzerland.

Hubbard, A., H. Blatter, P. Nienow, D. Mair, and B. Hubbard (1998), Comparison of a three-dimensional model for glacier flow with field data from Haut Glacier d'Arolla, Switzerland, *J. Glaciol.*, *44*(147), 368–378.

Iqbal, M. (1983), *An Introduction to Solar Radiation*, 390 pp., Academic, San Diego, Calif.

Justus, C. G., W. R. Hargraves, A. Mikhail, and D. Graber (1978), Methods for estimating wind speed frequency distributions, *J. Appl. Meteorol.*, *17*, 350–353.

Kasten, F. (1966), A new table and approximation formula for the relative optical air mass, *Arch. Meteorol. Geophys. Bioklimatol., Ser. B*, *14*, 206–223.

Klemes, V. (1985), Sensitivity of water resources systems to climate variation, *World Clim. Progr. Rep. 98*, World Meteorol. Org., Geneva, Switzerland.

Klok, E. J., and J. Oerlemans (2002), Model study of the spatial distribution of the energy and mass balance of the Morteratschgletscher, Switzerland, *J. Glaciol.*, *48*(163), 505–518.

Knap, W. H., B. W. Brock, J. Oerlemans, and I. C. Willis (1999a), Comparison of Landsat TM-derived and ground-based albedos of Haut Glacier d'Arolla, Switzerland, *Int. J. Remote Sens.*, *20*(17), 3293–3310.

Knap, W. H., C. H. Reijmer, and J. Oerlemans (1999b), Narrowband to broadband conversion of Landsat TM glacier albedos, *Int. J. Remote Sens.*, *20*(10), 2091–2110.

Kondratyev, K. Y. (1969), *Radiative Heat Exchange in the Atmosphere*, 411 pp., Academic, San Diego, Calif.

Mannstein, H. (1985), The interpretation of albedo measurements on a snow covered slope, *Arch. Meteorol. Geophys. Bioklimatol., Ser. B*, *36*, 73–81.

Nash, J. E., and J. V. Sutcliffe (1970), River flow forecasting through conceptual models, 1, a discussion of principles, *J. Hydrol.*, *10*(3), 282–290.

Niemelä, S., P. Räisänen, and H. Savijärvi (2001), Comparison of surface radiative flux parameterizations, Part II: Shortwave radiation, *Atmos. Res.*, *58*, 141–154.

Nunez, M. (1980), The calculation of solar and net radiation in mountainous terrain (Risdon Tasmania), *J. Biogeogr.*, *7*(2), 173–186.

Oerlemans, J., and B. Grisogono (2000), Glacier wind and parameterization of the related surface heat flux, *Tellus, Ser. A*, *54*, 440–452.

Oerlemans, J., et al. (1998), Modelling the response of glaciers to climate warming, *Clim. Dyn.*, *14*, 267–274.

Ohmura, A. (2001), Physical basis for the temperature-based melt-index method, *J. Appl. Meteorol.*, *40*, 753–761.

Pellicciotti, F., B. Brock, U. Strasser, P. Burlando, M. Funk, and J. Corripio (2003), An enhanced, albedo accounting, temperature-index melt model for distributed application, paper presented at International Symposium on Snow and Avalanches, Int. Glaciol. Soc., Davos, Switzerland.

Plüss, C., and R. Mazzoni (1994), The role of turbulent heat fluxes in energy balance of high alpine snow cover, *Nordic Hydrol.*, *25*, 25–28.

Prata, A. J. (1996), A new long-wave formula for estimating downward clear-sky radiation at the surface, *Q. J. R. Meteorol. Soc.*, *122*, 1127–1151.

Richter, R. (2001), Atmospheric and topographic correction: Model ATCOR3, *DLR Rep. DLR-IB 564-03/01*, Deutsches Zentrum für Luft- und Raumfahrt, Wessling, Germany.

Robinson, N. (Ed.) (1966), *Solar Radiation*, Elsevier Sci., New York.

Sauberer, F. (1955), Zur Abschätzung der Globalstrahlung in verschiedenen Höhenstufen der Ostalpen, *Wetter Leben*, *7*, 22–29.

Schulla, J. (1997), *Hydrologische Modellierung Von Flussgebieten zur Abschätzung der Folgen von Klimaänderungen*, 187 pp., Dept. of Geography, ETH Zurich, Zurich, Switzerland.

Schwerdtfeger, P. (1976), *Physical Principles of Micrometeorological Measurements, Develop. in Atmos. Sci.*, vol. 6, Elsevier Sci., New York.

Spencer, J. W. (1971), Fourier series representation of the position of the sun, *Search*, *2*, 171.

Strasser, U., and W. Mauser (2001), Modelling the Spatial and Temporal Variations of the Water Balance for the Weser Catchment 1965–1994, *J. Hydrol.*, *254*, 199–214.

U.S. Army Corps of Engineers (1956), *Snow Hydrology*, 437 pp., U.S. Army Corps of Eng., North Pac. Div., Portland, Oreg.

B. Brock, Department of Geography, University of Dundee, Dundee, DD1 4HN, Scotland.

P. Burlando, J. Corripio, and F. Pellicciotti, Institute of Hydromechanics and Water Resources Management, Section Hydrology and Water Resources Management, 8093 Zurich, Switzerland.

M. Funk, Laboratory of Hydraulics, Hydrology and Glaciology, Section Glaciology, 8092 Zurich, Switzerland.

U. Strasser, Department of Earth and Environmental Sciences, Section Geography, University of Munich, D-80333 Munich, Germany. (u.strasser@iggf.geo.uni-muenchen.de)